Off-axis low-energy structures in above-threshold ionization

M. Möller,[1,2,*] F. Meyer,[2] A. M. Sayler,[1,2] G. G. Paulus,[1,2] M. F. Kling,[3] B. E. Schmidt,[4] W. Becker,[5] and D. B. Milošević[5,6,7]

[1]*Helmholtz Institute Jena, Fröbelstieg 3, D-07743 Jena, Germany*

[2]*Institute of Optics and Quantum Electronics, Abbe Center of Photonics, Friedrich Schiller University, Max-Wien-Platz 1, D-07743 Jena, Germany*

[3]*Max Planck Institute of Quantum Optics, Hans-Kopfermann-Str. 1, D-85748 Garching, Germany*

[4]*Institut National de la Recherche Scientifique, Centre Energie Materiaux et Telecommunications, Varennes, Qc, J3X1S2, Canada*

[5]*Max-Born-Institut, Max-Born-Str. 2a, D-12489 Berlin, Germany*

[6]*Faculty of Science, University of Sarajevo, Zmaja od Bosne 35, 71000 Sarajevo, Bosnia and Herzegovina*

[7]*Academy of Sciences and Arts of Bosnia and Herzegovina, Bistrik 7, 71000 Sarajevo, Bosnia and Herzegovina*

(Received 13 March 2014; published 15 August 2014)

The velocity map of the above-threshold ionization electron spectrum at long laser wavelength exhibits a characteristic structure normal to the laser polarization, which has the appearance of a trident or a three-pronged fork. The forklike structure vanishes for few-cycle laser pulses. It is explained in terms of the classical-electron-trajectories model of strong-field ionization augmented so as to allow for rescattering. The analysis reveals its relation to the so-called low-energy structure, which was recently observed for very small transverse momenta.

DOI: 10.1103/PhysRevA.90.023412 PACS number(s): 33.80.Rv, 42.50.Hz

An atom exposed to an intense laser field provides one of the simplest physical realizations of a nonlinearly driven system. It has revealed various phenomena that have generated subfields of their own, such as the generation of high harmonics of the incident laser field, which in turn has brought us attosecond pulses [1]. In contrast to high-order harmonic generation, ionization of atoms can be investigated as a pure single-atom event; macroscopic effects have no significance. Especially, above-threshold ionization (ATI) has caught the interest of experimentalists and theorists alike, ever since its first observation 35 years ago [2,3]. ATI is characterized by the fact that the atom absorbs more photons than are necessary for ionization.

In view of the simplicity of the system in question—in principle, as simple as hydrogen [4]—it is remarkable that novel features of ATI have continued to emerge. Recent examples include frustrated tunneling ionization (FTI) [5] and a carpetlike pattern in the ionization velocity map at about right angle to the laser polarization [6] and, for comparatively long laser wavelengths, the so-called low-energy structure (LES) [7] and spiderlike interference structures (SPIDER) that were interpreted as holograms [9–11]. The most recent such examples include a structure with an energy below the LES, the very-low-energy structure [12] and a strong enhancement at practically zero energy [13]. The latter two are assumed to be Coulomb-related effects, but there is no consensus as to their detailed origin. ATI is also the basis of various applications: For example, analysis of the velocity map at high energy allows one to extract the electron-ion scattering potential [14] while the details of the spider structure are sensitive to the atomic potential [11]. It also has been used to measure the carrier-envelope phase of few-cycle pulses [15,16].

In this letter, strong-field ionization into states with low electron energy by a long-wavelength laser field is investigated experimentally and modeled theoretically. We compare the velocity map of the electron spectrum which is generated by a long laser pulse with the one generated by a few-cycle pulse. Besides retrieving the LES and the SPIDER, we observe a third–so far unadressed–fork-like structure which has a shape reminiscent of a trident or three-pronged fork (from here on, we will refer to it by the fork). The fork appears at close to right angle to the laser polarization axis, gets more pronounced if the laser wavelength is increased, and is very sensitive to the pulse duration.

While seeking a theoretical explanation for the fork, we find that the low-energy features mentioned can be explained qualitatively in terms of classical electron trajectories in the presence of the laser field only [17]. The model is augmented by two features: one single act of rescattering into arbitrary angles is included as well as trajectories that are substantially longer than one optical cycle [18]. This puts the LES and the fork on the same footing as high-energy features such as, e.g., the plateau. There is, however, one important difference: high electron energies, which form the plateau, can only be reached by rescattering while low-energy rescattering features have to compete with the smooth contribution of the direct electrons, which do not rescatter at all. It is here where the Coulomb potential comes in: The divergent Coulomb forward scattering cross section enhances the LES and the fork so that they become visible in the total spectrum. Since the quantum-mechanical strong-field approximation (SFA) builds on the aforementioned electron orbits [19], the SFA describes the low-energy features very well as we will demonstrate.

In contrast to previous analyses [20–24], which identify the Coulomb potential as the sole origin of the LES, we conclude that the LES exists, in principle, for any potential. For a qualitative understanding of rescattering at low energies, inclusion of a scattering potential is needed only in the sense that it is required to act as scattering center for rescattering electrons. This intuitive and surprisingly simple insight is of central importance for self-probing approaches in imaging of ultrafast dynamics such as, e.g., laser-induced electron diffraction [8] where differential scattering cross sections are extracted from the velocity map of the above-threshold ionization electron spectrum [14].

*max.moeller@uni-jena.de

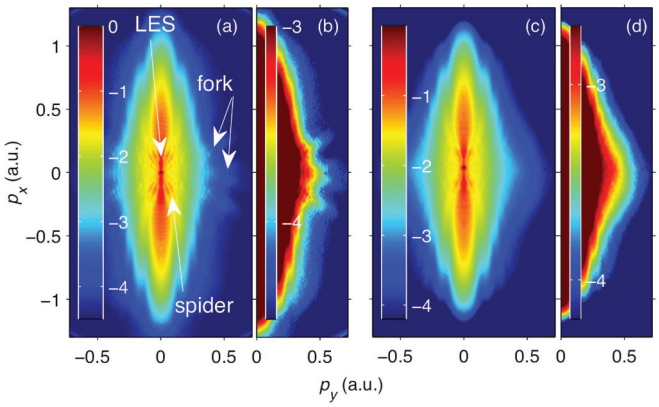

FIG. 1. (Color online) The logarithm of the photoelectron momentum distribution of the ionization of Xe by a 75-fs (12.5 cycles) laser pulse with 1.8-μm center wavelength. The structure of interest is around $p_y \sim \pm 0.5$ a.u. The labels with arrows mark the characteristic features that are observed at long wavelength, i.e., the LES, the spiderlike structure, and the fork. Panels (c) and (d) show the same as (a) and (b) but for an 11-fs (2 cycles) laser pulse. In (b) and (d), the color scale is clipped from the side with the high count rate for better visibility of the fork. The carrier-envelope phase is not fixed and the peak intensity was around 8×10^{13} W/cm^2 for both.

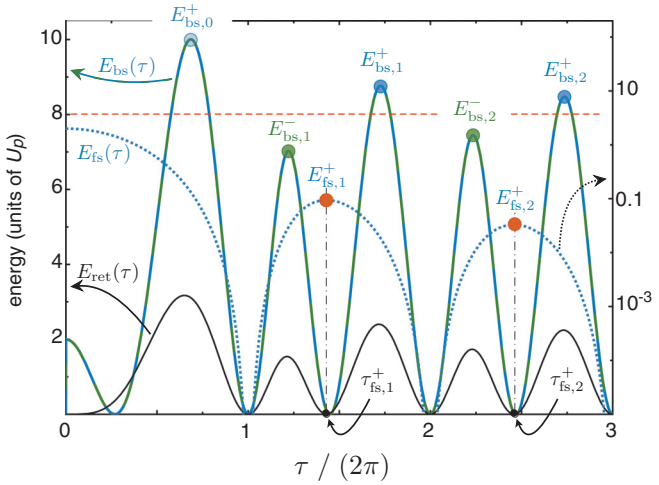

FIG. 2. (Color online) The return energy E_{ret} [thin solid (black) line, scale on the left], the back-scattering energy E_{bs} [thick solid (blue/green) line, scale on the left], and the forward scattering energy E_{fs} [dotted (blue) line, logarithmic scale on the right] as given by Eq. (1) in units of U_p as functions of the travel time τ. The various maxima are labeled as defined in the text. The horizontal dashed (red) line at 8 U_p marks the border between the energies $E^+_{bs,n}$ and $E^-_{bs,n}$. The orange dots emphasize the two LES energies (also marked in Fig. 3). The extremal energies $E^-_{fs,n}$ of the second ("−") family are identically 0 as the respective trajectories start and return at the extrema of the field with $\tau^-_{fs,n} = n\pi (n = 1,2,\dots)$. Note [by calculation from Eq. (1) or by inspection] that at the times $\tau \equiv \tau^+_{fs,n}$ we have $E_{ret} = 0$, $E_{bs} = E_{fs}$, and E_{fs} assumes a maximum, which is given by $E^+_{fs,n}$.

Although the fork has gone unaddressed until now, reexamination also reveals the fork structure in some previous experiments [9–11,25–27]. In the current work, the fork is observed by ionizing Xe atoms using the output of an optical parametric amplifier with a center wavelength of 1.4–2.2 μm. Photoelectron momentum distributions are measured using a velocity-map imaging (VMI) spectrometer [28]. Employing spectral broadening in a hollow-core fiber and bulk compression [29,30] allows studying the momentum distributions for both long laser pulses consisting of roughly 13 optical cycles and for few-cycle pulses with a duration down to less than two cycles [full width at half maximum (FWHM) of the intensity [31]]. For the latter, only 1.8-μm center wavelength is available to which we restrict the discussion.

Figures 1(a) and 1(b) show typical momentum distributions obtained for a long pulse duration of 75 fs (12.5 cycles) at $(8 \pm 3) \times 10^{13}$ W/cm^2 peak intensity. The fork structure is identified as the prominent prongs with large transverse momenta that appear symmetrically around zero parallel momentum. The prongs are more clearly pronounced the longer the wavelength. A closer look reveals that the middle prong is in fact a twin prong. Beside the fork, the measurements show the typical LES [7] and the spiderlike structures [11]. For few-cycle pulses, the fork structure is washed out beyond recognition [see Figs. 1(c) and 1(d)].

We will present an explanation of the fork in the context of the model of classical orbits and its quantum-mechanical version, the strong-field approximation (SFA) [32], both augmented to allow for rescattering [33,34]. In the classical model, the electron enters the continuum at the ionization time t_0. An electron liberated at this time may either directly go to the detector without any interaction with its parent ion (a so-called "direct electron") or it may be driven by the field into a recollision with its parent ion and elastically scatter. The time t_r of the recollision is a (multivalued) function of t_0. In the recollision, the electron may scatter in any direction; the limiting cases are back scattering (when the electron changes its direction of motion by 180°), which may generate high final energy, and forward scattering (when the electron maintains its momentum), which implies low final energy.

For a monochromatic plane wave with the electric field $\mathbf{E}(t) = \hat{\mathbf{x}}\omega A_0 \cos(\omega t + \phi)$, the energy of the returning recolliding electron E_{ret} and the final energies of back scattering E_{bs} and forward scattering E_{fs} can be calculated from the classical model as functions of their "travel time" $\tau \equiv \omega(t_r - t_0)$ [35,36]:

$$E_{ret} = 2U_p(2 - 2\cos\tau - \tau\sin\tau)^2 f(\tau), \quad (1a)$$

$$E_{bs} = 2U_p(3 - 3\cos\tau - 2\tau\sin\tau)^2 f(\tau), \quad (1b)$$

$$E_{fs} = 2U_p(1 - \cos\tau)^2 f(\tau), \quad (1c)$$

with $f(\tau) = (2 + \tau^2 - 2\cos\tau - 2\tau\sin\tau)^{-1}$ and the ponderomotive potential $U_p = A_0^2/4$. These energies are plotted in Fig. 2. The back-scattered energy displays a series of maxima, starting with the well-known high-energy ATI cutoff at $E^+_{bs,0} = 10.01\,U_p$ and followed by lower maxima at $E^-_{bs,n} < 8\,U_p$ and $E^+_{bs,n} > 8\,U_p$ $(n = 1,2,\dots)$. The forward scattering energy also shows a series of maxima at the energies $E^+_{fs,n}$ $(n = 1,2,\dots)$ starting with $E^+_{fs,1} = 0.094\,U_p$ at $\tau \equiv \tau^+_{fs,1} = 8.99$, $E^+_{fs,2} = 0.033\,U_p$ at $\tau^+_{fs,2} = 15.5$, etc. These are the energies of the LES [7], and the values given here agree with the soft-recollision model of Refs. [23,24].

Now, maxima of $E_{\rm bs}$ and $E_{\rm fs}$ correspond to cutoffs in the electron energy spectrum in the direction of the laser polarization. In reality and in a quantum description such as the SFA, the cutoffs are smoothed. The highest cutoff of $10.01\,U_{\rm p}$ marks the end of the rescattering plateau, while the lower cutoffs may or may not be visible as they are competing with other (noncutoff) contributions. In this respect, it is of decisive importance to note that, for a Coulomb potential, the forward-scattering cross section is large (actually, divergent), and this divergence is especially strong for $E_{\rm ret}=0$. This allows the LES to rise above the contribution of the direct electrons. As mentioned, the respective electron energies are given by the forward-scattering cutoffs $E^{+}_{{\rm fs},n}$.

For rescattering in an arbitrary direction characterized by the angle θ in the laboratory frame [$\mathbf{p}=p(\theta)(\cos\theta,\sin\theta)$] the energies are given by [35,36]

$$E_{\rm kin}(\theta)=E_{\rm ret}\left[g(\tau)\cos\theta\pm\sqrt{1-g^2(\tau)\sin^2\theta}\right]^2, \qquad (2)$$

with $g(\tau)=(1-\cos\tau-\tau\sin\tau)/(2-2\cos\tau-\tau\sin\tau)$. For $\theta=0$ and $\theta=\pi$ they reduce to Eqs. (1c) and (1b). For fixed angle θ, the corresponding cutoff energies that arise upon variation of the travel time, i.e., the maxima of $E_{\rm kin}(\theta)$, are plotted in Fig. 3 in the (p_x,p_y) plane.

For large $|p_x|$, on the p_x axis we recognize the maximal classical momenta coming from back scattering to the energies $E^{+}_{{\rm bs},0}=10.01\,U_{\rm p}$ and $E^{+}_{{\rm bs},n}$ and $E^{-}_{{\rm bs},n}$ $(n=1,2,\dots)$ (corresponding to the maxima of $E_{\rm bs}$ in Fig. 2). Near the center of the figure, for positive and for negative momenta p_x and for $p_y=0$, we retrieve the LES energies $E^{+}_{{\rm fs},n}$, which are marked by orange dots. The various curves connect the cutoffs of the back-scattering energy $E_{\rm bs}$ with those of the forward-scattering energy $E_{\rm fs}$, thus justifying the notation of two distinct families of cutoffs introduced above.

It should be noted that the cutoff energies do not form exact circles as reported in [37], where the dependence of the τ_n on the scattering angle θ was neglected. Rather, they assume dropletlike shapes. We shall refer to the curves that intersect the p_x axis at the energies $E^{+}_{{\rm bs},n}>8\,U_{\rm p}$ ($E^{-}_{{\rm bs},n}<8\,U_{\rm p}$) as the $>8\,U_{\rm p}$ ($<8\,U_{\rm p}$) droplets. As explained above, the $>8\,U_{\rm p}$ droplets connect with the LES energies while the $<8\,U_{\rm p}$ droplets all pass through the origin. The two sets are separated by two limit curves (dotted in Fig. 3), one with $p_x>0$ and the other with $p_x<0$, which are exact circles. The intersections of the $>8\,U_{\rm p}$ droplets form a pattern of nested diamonds (rhombi). The outermost diamond (with its corner points on the p_x axis at $\pm A_0$) reproduces the diamondlike structure observed in calculations presented in Figs. 3(b) and 3(c) of [9]. In the present context, however, the $10\,U_{\rm p}$ droplets do not play a role. For $p_x=A_0, p_y=0$, e.g., the corresponding trajectory starts at a zero transition of the field and has zero travel time.

The fork and the LES relate to the central part of Fig. 3, which is enclosed by the orange ellipse. The just mentioned two limit curves separate a region outside the figure "8," which is formed by the limit curves, from two disk-shaped regions inside the figure "8." The first contains the middle prong of the fork while the outer prongs are located in the disk-shaped regions. We shall return to this below when we compare Fig. 3 with the SFA simulations.

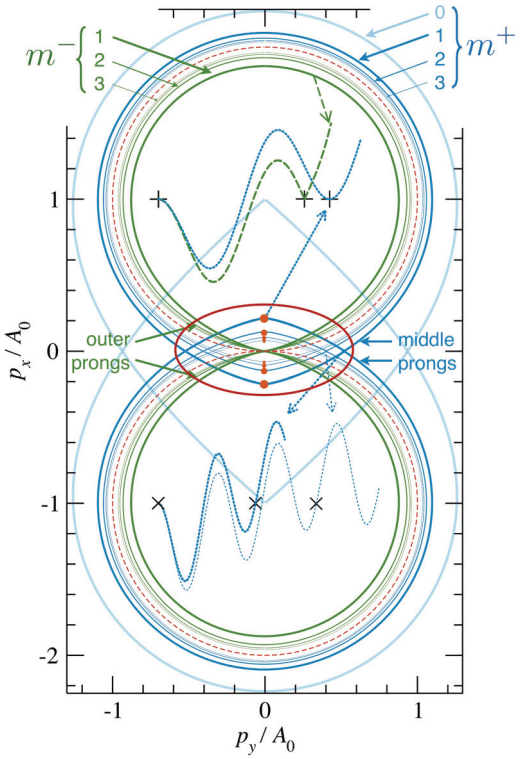

FIG. 3. (Color online) Angle-dependent cutoffs of the electron drift energy $E_{\rm kin}(\theta)=p^2(\theta)/2$, Eq. (2). On the p_x axis, we see the cutoffs corresponding to $10.01\,U_{\rm p}$ and then to $8.77\,U_{\rm p}$,$8.48\,U_{\rm p}$, etc. (blue curves, labeled $m^+=0,1,2,\dots$) above $8\,U_{\rm p}$, and to $7.03\,U_{\rm p}$,$7.45\,U_{\rm p}$, etc. (green curves, labeled $m^-=1,2,\dots$) below $8\,U_{\rm p}$. The two sets converge to two "limit circles," one for $p_x>0$ and the other for $p_x<0$, which intersect the vertical axis at $p_x=\pm\sqrt{2\times 8\,U_{\rm p}}=2A_0$ and are represented by the dashed (red) curves. They are exact circles and are tangential to the horizontal axis at the origin. Near the origin, for $p_y=0$, we see the LES energies at $0.094\,U_{\rm p}$,$0.033\,U_{\rm p}$,... marked by solid circles (orange). The two insets show several longitudinal electron trajectories. For details see the text. The orange ellipse at the center of the figure identifies the region relevant for the fork.

The two insets in Fig. 3 present projections of some relevant electron trajectories on the x axis (the x axis is up, the t axis is horizontal). The electron starts at the position $(x,t)=(0,0)$ which is given by "+" or "×" and rescatters at times $t_{\rm r}$ at the position indicated by the same symbol. The arrows identify the final drift momentum (p_x,p_y) of each trajectory. We start with the dashed (green) trajectory in the upper inset, which represents an example of the familiar case of back scattering. For the present example, the final drift momentum is located on the inner circle ($E=E^{-}_{{\rm bs},1}=7.03\,U_{\rm p}$ for exact back scattering) and makes the angle $\theta=10^\circ$ with respect to the x axis. The other three trajectories are forward scattered. The second trajectory in the upper inset corresponds to the LES with the energy $E^{+}_{{\rm fs},1}=0.094\,U_{\rm p}$. The two trajectories in the lower inset also belong to the family of trajectories with maximum back-scattering energies $>8\,U_{\rm p}$. The trajectories displayed are located on the off-axis extension of the LES with $n=1$ (thick curve) and $n=2$ (longer thin curve) and contribute to the middle prong of the fork.

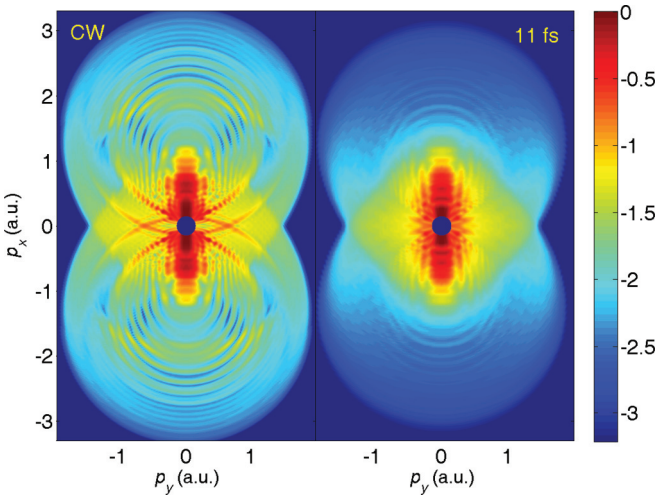

FIG. 4. (Color online) The logarithm of the differential ionization yield (in arb. units) of Xe presented in false colors in the electron momentum plane for ionization by a linearly polarized laser pulse having the wavelength 1.8 μm and the intensity 5×10^{13} W/cm^2. The left panel is calculated for an infinitely extended monochromatic plane wave (CW); the right panel is for a finite pulse of five optical cycles total duration (11 fs FWHM) with a $\cos^2$ envelope and averaged over the carrier-envelope phase. Focal averaged results are obtained using the improved SFA (with both direct and rescattered electrons). Note that the fork is washed out for the short pulse while it is clearly visible for the cw pulse.

To calculate the velocity map for ionization of Xe shown in Fig. 4 we use focal-averaged SFA [38]. First, it is important to note that the most intense ellipsoid-shaped central region, which is elongated in the x direction of the plot, is due to the direct electrons. Near the origin, the direct electrons cover the structures predicted by Fig. 3 completely, including the LES [39]. Scattering can only be identified outside this region, for about $|p_y| \gtrsim 0.3$ a.u. There, we see two arcs emanating from the direct-electron region, which intersect each other at $|p_y| \approx 0.7$ a.u. They correspond to the $>8\,U_\mathrm{p}$ droplets and define the end of the diamond-shaped region. They are due to the off-axis extension of the LES and form the middle prong of the fork. We also see, on either side, two additional arcs, which are due to the $<8\,U_\mathrm{p}$ droplets. These form the two outer prongs of the fork. This interpretation of the fork is further supported by the experimental observation that the fork structure is absent for few-cycle pulses that naturally do not support trajectories with extended travel time. The same conclusion was already drawn for the LES from the soft-recollision model [24].

In conclusion, we presented experimental velocity maps of ATI of xenon by an infrared laser. We observed a pronounced three-pronged forklike structure in the transverse direction and traced it to rescattering. We identified the electron orbits responsible for this structure and confirmed this interpretation by simulations using the strong-field approximation. We found that the fork structure is intimately related to the low-energy structure: The former constitutes the off-axis extension (to nonzero transverse momenta) of the latter.

Especially, we made the case that both the fork and the LES are not primarily caused by the Coulomb field [40]. They exist already on the level of classical laser-field-only trajectories, regardless of the binding potential. For short-range potentials, rescattering and its pertinent structures have a low yield so that they are not visible on the background of the direct electrons. The Coulomb potential, owing to its large (divergent) forward-scattering cross section, acts as a magnifier, which enhances these structures to the extent that they dominate the direct-electron contributions [41]. We conjecture that the fork and the LES are universal structures in the sense that they depend only weakly on the details of the binding potential. We thus present a unified picture of ATI at all electron energies in the context of the well-established classical trajectories and the strong-field approximation. This may also set the stage for the origin of the very-low-energy structure [12] and the zero-energy structure [13].

We gratefully acknowledge support by the Alexander von Humboldt Foundation, the German Federal Ministry of Education and Research in the framework of the Research Group Linkage Programme, and the German Research Foundation [(DFG) Grants No. PA730/4 and No. SFB/TR18].

[1] F. Krausz and M. Ivanov, Rev. Mod. Phys. **81**, 163 (2009).
[2] P. Agostini, F. Fabre, G. Mainfray, G. Petite, and N. K. Rahman, Phys. Rev. Lett. **42**, 1127 (1979).
[3] P. Agostini and L. F. DiMauro, Adv. At. Mol. Opt. Phys. **61**, 117 (2012).
[4] G. G. Paulus, W. Nicklich, F. Zacher, P. Lambropoulos, and H. Walther, J. Phys. B **29**, L249 (1996).
[5] T. Nubbemeyer, K. Gorling, A. Saenz, U. Eichmann, and W. Sandner, Phys. Rev. Lett. **101**, 233001 (2008).
[6] Ph. A. Korneev *et al.*, Phys. Rev. Lett. **108**, 223601 (2012); Ph. A. Korneev, S. V. Popruzhenko, S. P. Goreslavski, W. Becker, G. G. Paulus, B. Fetić, and D. B. Milošević, New J. Phys. **14**, 055019 (2012).
[7] C. I. Blaga, F. Catoire, P. Colosimo, G. G. Paulus, H. G. Muller, P. Agostini, and L. F. DiMauro, Nature Phys. **5**, 335 (2009); W. Quan *et al.*, Phys. Rev. Lett. **103**, 093001 (2009).
[8] C. I. Blaga *et al.*, Nature (London) **483**, 194 (2012).
[9] Y. Huismans *et al.*, Science **331**, 61 (2011).
[10] X.-B. Bian, Y. Huismans, O. Smirnova, K.-J. Yuan, M. J. J. Vrakking, and A. D. Bandrauk, Phys. Rev. A **84**, 043420 (2011); T. Marchenko, Y. Huismans, K. J. Schafer, and M. J. J. Vrakking, *ibid.* **84**, 053427 (2011).
[11] D. D. Hickstein *et al.*, Phys. Rev. Lett. **109**, 073004 (2012).
[12] C. Y. Wu, Y. D. Yang, Y. Q. Liu, Q. H. Gong, M. Wu, X. Liu, X. L. Hao, W. D. Li, X. T. He, and J. Chen, Phys. Rev. Lett. **109**, 043001 (2012).
[13] J. Dura *et al.*, Sci. Rep. **3**, 2675 (2013).
[14] C. D. Lin, A.-T. Le, Z. Chen, T. Morishita, and R. Lucchese, J. Phys. B **43**, 122001 (2010).
[15] A. M. Sayler, T. Rathje, W. Müller, K. Rühle, R. Kienberger, and G. G. Paulus, Opt. Lett. **36**, 1 (2011).

[16] S. Micheau, Z. Chen, A. T. Le, J. Rauschenberger, M. F. Kling, and C. D. Lin, Phys. Rev. Lett. **102**, 073001 (2009).
[17] H. B. van Linden van den Heuvell and H. G. Muller, in *Multiphoton Processes*, edited by S. J. Smith and P. L. Knight (Cambridge University Press, Cambridge, 1987), pp. 25–34; in the literature, this model has often been referred to by the simple-man model.
[18] G. G. Paulus, W. Becker, W. Nicklich, and H. Walther, J. Phys. B **27**, L703 (1994).
[19] W. Becker, F. Grasbon, R. Kopold, D. B. Milošević, G. G. Paulus, and H. Walther, Adv. At. Mol. Opt. Phys. **48**, 35 (2002).
[20] C. Liu and K. Z. Hatsagortsyan, Phys. Rev. Lett. **105**, 113003 (2010).
[21] T. M. Yan, S. V. Popruzhenko, M. J. J. Vrakking, and D. Bauer, Phys. Rev. Lett. **105**, 253002 (2010).
[22] C. Lemell, K. I. Dimitriou, X.-M. Tong, S. Nagele, D. V. Kartashov, J. Burgdörfer, and S. Gräfe, Phys. Rev. A **85**, 011403(R) (2012).
[23] A. Kästner, U. Saalmann, and J. M. Rost, Phys. Rev. Lett. **108**, 033201 (2012).
[24] A. Kästner, U. Saalmann, and J. M. Rost, J. Phys. B **45**, 074011 (2012).
[25] B. Bergues, S. Zherebtsov, Y. Deng, X. Gu, I. Znakovskaya, R. Kienberger, F. Krausz, G. Marcus, and M. F. Kling, New J. Phys. **13**, 063010 (2011).
[26] A. von Veltheim, B. Manschwetus, W. Quan, B. Borchers, G. Steinmeyer, H. Rottke, and W. Sandner, Phys. Rev. Lett. **110**, 023001 (2013).
[27] M. Weger, J. Maurer, A. Ludwig, L. Gallmann, and U. Keller, Opt. Express **21**, 21981 (2013).
[28] A. T. J. B. Eppink and D. H. Parker, Rev. Sci. Instrum. **68**, 3477 (1997).
[29] B. E. Schmidt, A. D. Shiner, P. Lassonde, J.-C. Kieffer, P. B. Corkum, D. M. Villeneuve, and F. Legaré, Opt. Express **19**, 6858 (2011).
[30] P. Béjot, B. E. Schmidt, J. Kasparian, J.-P. Wolf, and F. Legaré, Phys. Rev. A **81**, 063828 (2010).
[31] See Sec. 4.3 in D. B. Milošević, G. G. Paulus, D. Bauer, and W. Becker, J. Phys. B **39**, R203 (2006).
[32] L. V. Keldysh, Zh. Eksp. Teor. Fiz. **47**, 1945 (1964) [Sov. Phys. JETP **20**, 1307 (1964)]; F. H. M. Faisal, J. Phys. B **6**, L89 (1973); H. R. Reiss, Phys. Rev. A **22**, 1786 (1980).
[33] W. Becker, A. Lohr, and M. Kleber, J. Phys. B **27**, L325 (1994); corrigendum J. Phys. B **28**, 1931 (1995).
[34] D. B. Milošević and F. Ehlotzky, Phys. Rev. A **58**, 3124 (1998).
[35] R. Kopold, Ph.D. thesis, Technische Universität München, 2001.
[36] E. Hasović, M. Busuladžić, A. Gazibegović-Busuladžić, D. B. Milošević, and W. Becker, Laser Phys. **17**, 376 (2007).
[37] D. Ray *et al.*, Phys. Rev. Lett. **100**, 143002 (2008).
[38] For a review of classical and quantum orbits in the context of the SFA, see Ref. [19]; for the focal-averaging method, see Ref. [36]. The on-axis LES was confirmed and investigated in this context by D. B. Milošević, Phys. Rev. A **88**, 023417 (2013).
[39] This is because the calculation employed a short range rather than the full unscreened Coulomb potential, thereby avoiding the aforementioned divergence in the forward direction.
[40] It was shown previously by numerical evaluation by L. Guo, S. S. Han, X. Liu, Y. Cheng, Z. Z. Xu, J. Fan, J. Chen, S. G. Chen, W. Becker, C. I. Blaga, A. D. DiChiara, E. Sistrunk, P. Agostini, and L. F. DiMauro, Phys. Rev. Lett. **110**, 013001 (2013), that the SFA yields the LES.
[41] Coulomb rescattering was calculated in Ref. [34] but little attention was paid at the time to the low-energy part of the spectrum.